Influence of Microstructure on Corrosion Properties of Fe–V Alloy from Vanadium Slag

Weibin Wang[1,2,3] · Wei Wang[1,2,3] · Qirui Sun[1,2,3]

Abstract

Four types of multiphase Fe–V alloys were examined, comprising ferrite, pearlite, and bainite microstructures. Electrochemical impedance spectroscopy and potentiodynamic polarization were employed to study the effect of microstructure on electrochemical properties of the alloys in 3.5% NaCl solution. The cathode reaction was found to be the main step controlling the corrosion dissolution process. The lowest corrosion current density ($2.104\ \mu A/cm^2$) for the Fe–V alloy with bainite indicated that it had outstanding corrosion resistance. Although an increase in pearlite content had a negative effect on corrosion resistance of the alloy, refinement of the lamellar spacing had the opposite effect. Surface corrosion morphologies were observed by scanning electron microscopy. The results indicate that fine cementite uniformly distributed in the bainite promoted slight uniform dissolution of ferrite. Corrosion and dissolution that occurred at the junctions of the pearlite colonies with different directions was more severe. The increase of content of V effectively improved the corrosion resistance of Fe–V alloy. Compared with the matrix, the VC precipitated phase was cathodically protected in the electrochemical corrosion process by virtue of its positive corrosion potential.

Keywords Fe–V alloy · Electrochemical corrosion · Pearlite · Bainite · VC

1 Introduction

Vanadium is an important strategic resource. As a widely used alloying element, vanadium can form binary or ternary alloys with Al, Fe, Ti, Mn, and other metals. Vanadium-containing alloys have excellent properties and can be used in various fields, including aerospace, energy, transportation, and the chemical industry [1]. The extensive application of vanadium alloys is attributed to its outstanding mechanical properties, favorable corrosion resistance, low biological hazard safety risk, and environmentally benign nature [2, 3].

In recent years, with a focus on micro-alloyed iron and steel materials, vanadium is becoming more widely used in cast iron. The presence of vanadium in iron and steel leads to a remarkable improvement in the plasticity, ductility, flexibility, and strength of these materials, resulting in use of Fe–V alloys in bridge structures, pipelines, and railway tracks [4].

Recent studies of vanadium alloys involve binary and ternary systems. Vanadium-containing iron-based alloys are responsible for major investigations. Kawalec and Fraś [5] observed the microstructures of a series of Fe–C–V alloys with different chemical compositions by optical metallographic techniques. The results indicated that the matrix in high-vanadium cast iron comprised mainly ferrite, lamellar pearlite, granular pearlite, and their mixtures. The type of matrix determined the mechanical properties and wear resistance of high-vanadium cast iron. Xu et al. [6] reported that a suitable carbon content in Fe–V–Cr–Mo alloy is 2.58%. The appearance of nearly spherical VC and lath martensite endowed the alloy with moderate hardness and favorable wear resistance. Kawalec and Górny [7] reported that spheroidizing treatment of VC in Fe–C–V alloy could improve the mechanical properties by 60%. The mass wear rate of high-vanadium cast iron is nearly half that of

✉ Wei Wang
   wwlyzwkj@126.com

1 College of Materials Science and Engineering, Henan University of Science and Technology, Luoyang 471023, Henan, People's Republic of China

2 Collaborative Innovation Center of Nonferrous Metals Henan Province, Luoyang 471023, Henan, People's Republic of China

3 Henan Key Laboratory of Non-Ferrous Materials Science and Processing Technology, Luoyang 471023, Henan, People's Republic of China

wear-resistant cast steel. Notwithstanding, understanding of vanadium-containing cast iron is not yet fully clarified. To better understand the properties of vanadium-containing iron-based alloys, more comprehensive research is needed. Few reports have focused on the corrosion of vanadium-containing iron-based alloys. Available literature indicates that vanadium as a common alloying element not only displays excellent corrosion resistance in gases, salts, and water, but vanadium and its carbide show high stability in chloride solution [8, 9].

Corrosion susceptibility of alloy materials is largely affected by the morphology of the microstructure, as reported by several researchers [10–12]. Microstructure characteristics can be modified using alloying elements to improve the corrosion performance [13]. The Fe–V alloy phase diagram indicates that adding vanadium to pure iron can seal the austenite region and enlarge the ferrite region. Previous studies also demonstrated that vanadium can delay the transformation of pearlite and refine its interlamellar spacing [14, 15]. The type, number and distribution of phases caused by alloying element V can play an important role in the microstructure and corrosion resistance of Fe–V alloys. To our knowledge, rarely has been seen about the influence of alloying elements Cr and Mn on the microstructure and electrochemical performance of Fe–V alloy. In this paper, the corrosion behavior of Fe–V alloy in 3.5% NaCl solution was characterized by electrochemical workstation. In addition, the influence of galvanic effect between carbide and matrix on the corrosion performance of Fe–V alloy was also elucidated. The results of this study provide certain corrosion data for multiphase Fe–V alloys that will assist in preparing Fe–V alloys with favorable properties.

2 Experimental

2.1 Materials

In previous work, Fe–V alloy was successfully prepared from vanadium slag and high iron red mud [16]. The chemical analysis of the samples to be tested is listed in Table 1. However, the influence of microstructure on the electrochemical properties of Fe–V alloy has not been studied in detail. Therefore, four different Fe–V alloys with representative microstructures were selected from the previous work and denoted as Samples 1, 2, 3, and 4 in this study.

2.2 Microstructure

The specimens were mounted in epoxy resin, leaving only the bottom of the metal surface as the effective working area for contact with the electrolyte. Prior to the tests, the working surface of each sample was ground and polished to a mirror finish using a sequential series of emery papers (grit size 400–1200) and water-soluble diamond grinding paste with a particle size 1.5 μm, followed by cleaning in alcohol and drying using a blow dryer. The samples were etched with 4% Nital solution (96 mL ethanol, 4 mL nitric acid) and their microstructures observed by an Olympus PMG3 optical microscopy (OM) and a JSM-7800F field-emission scanning electron microscopy (FE-SEM) prior to the electrochemical experiments.

2.3 Electrochemical Measurements

The electrochemical performance of the samples was analyzed using an electrochemical workstation (Autolab PGSTAT 128N) connected to a three-electrode system. Experiments were performed in 3.5% NaCl solution at 25 °C. A graphite electrode, saturated calomel electrode, and the alloy samples were used as the counter, reference, and working electrodes, respectively. The samples were immersed in the electrolyte for about 60 min prior to electrochemical impedance spectroscopy (EIS) tests to obtain the stable open-circuit potential (OCP). EIS tests were performed at the corresponding OCP values, with a scanning frequency range from 10^5 to 10^{-1} Hz and the amplitude of 5 mV. Nova 1.10 software was used to analyze the impedance data and fit the corresponding equivalent circuit. Polarization curves were obtained in the potential scanning range of -250 to $+400$ mV (relative to the OCP) at a scanning rate of 1 mV/s. The corrosion morphologies of the samples after the polarization tests were evaluated by FE-SEM.

Table 1 Chemical analysis of four samples

Sample	Element content/mass%						
	Fe	V	C	Cr	S	Si	Mn
1	83.37	6.91	4.19	3.11	0.08	0.60	1.74
2	83.03	8.12	3.64	2.99	0.09	0.52	1.61
3	82.47	9.37	3.58	2.63	0.08	0.49	1.38
4	81.95	11.04	2.94	2.27	0.06	0.35	1.39

3 Results and Discussion

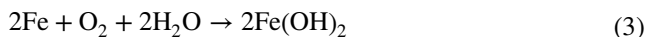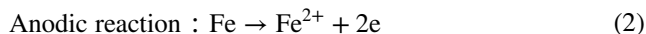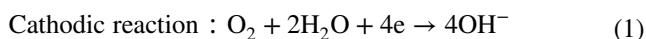### 3.1 Microstructural Observation

Microstructures of the four samples are shown in Fig. 1a–h. With the increase of content of alloying element V, the microstructure of the samples varied remarkably. Figure 1a indicates the microstructure of Sample 1 by OM. The distribution of pearlite (dark phase) is larger than that of ferrite (white). The insert of Fig. 1b shows that the pearlite was composed of lamellar ferrite and cementite. Microstructures similar to that of Sample 1 were found in Samples 2 and 3 (Fig. 1c–f); however, there were differences in the fractions of ferrite and pearlite, as well as interlamellar spacing of the pearlite. Compared with Sample 1, the area fraction (%) of ferrite gradually increased in Samples 2 and 3, whereas that of pearlite gradually decreased. The finer interlamellar spacing of pearlite is better identified from FE-SEM micrographs (shown as inserts of Fig. 1b, d, f). Three different areas of each sample's optical micrographs were selected to analyze and calculate the average area fraction and interlamellar spacing of pearlite phase by Image J software. The results are indicated in Table 2. Figure 1g, h show that the microstructure of Sample 4 mainly comprised bainite and bulk ferrite. In addition, the combination of vanadium and carbon promoted the formation of a VC precipitation phase, observed in the microstructures of all samples (Fig. 1a–h).

As shown in Table 1, the tested samples mainly contain three alloying elements, i.e. V, Cr and Mn. The V content of Sample 4 was nearly twice as high in Sample 1. However, the contents of Cr and Mn varied in a narrow range about 2.27–3.11 wt% and 1.38–1.74 wt%, respectively. The microstructure differences of the tested samples in Fig. 1 can be mainly attributed to the alloy composition. There are two reasons for this. On the one hand, the decrease in the content of C reduced the amount of pearlite. On the other hand, V and Cr can not only slow down the growth of pearlite but make the nose of continuous cooling transformation (CCT) curves move to the right and increase the degree of undercooling [17, 18]. Therefore, these result in the formation of less and finer pearlite structures under the same cooling condition (Fig. 1). Whereas Mn can decrease the eutectoid transformation temperature of pearlite, which hindered the refinement of the interlamellar spacing of pearlite [19]. The combined effect of alloying elements (V, Cr and Mn) promoted the refinement of pearlite structure (Table 2).

3.2 Polarization Curves

To study the corrosion resistance of these Fe–V alloys, potentiodynamic polarization curves of the four samples in

3.5% NaCl solution are shown in Fig. 2. The polarization curves all assumed a similar trend: the corrosion current density decreased as the corrosion potential increased in the positive direction in the cathodic polarization region. The anodic polarization curves showed a typical active dissolution zone without any signs of passivation, indicating that active corrosion of the electrode surfaces of all samples occurred in 3.5% NaCl solution, i.e., the anodic dissolution reaction of Fe [3]. Compared with Sample 1, the anodic polarization curves for the other samples shifted by varying degrees, suggesting that the anodic polarization current density decreased at the same polarization potential, i.e., the anodic reaction was limited to some extent and the corrosion rate slowed down. The main electrochemical reactions are as follows:

$$\text{Cathodic reaction}: O_2 + 2H_2O + 4e \rightarrow 4OH^- \quad (1)$$

$$\text{Anodic reaction}: Fe \rightarrow Fe^{2+} + 2e \quad (2)$$

$$2Fe + O_2 + 2H_2O \rightarrow 2Fe(OH)_2 \quad (3)$$

Kinetic information, such as the corrosion potential (E_{corr}) and corrosion current density (I_{corr}), can be determined by data-fitting in the strong-polarization Tafel region of the polarization curves. The specific parameters are presented in Table 3. There was no dramatic change in the cathodic slope β_c (in the range from 0.112 to 0.291) or anodic slope β_a (from 0.051 to 0.083) of the polarization curves, suggesting that the corrosion reaction mechanism for all samples were the same in this electrolyte. In general, the higher value of β_c compared with β_a indicates that cathodic control dominated the electrode reaction process. As a corrosion kinetic parameter, the variation of I_{corr} is opposite to the resistance of the electrochemical corrosion reaction [20]. A lower I_{corr} means that a sample is less prone to corrosion and dissolution. The data in Table 2 show that the values of I_{corr} gradually decreased; therefore, the corrosion rates could be ranked in descending order as follows: Sample 1, Sample 2, Sample 3, Sample 4. It indicated that the corrosion resistance of Fe–V alloy with bainite-ferrite structure was better than that with pearlite-ferrite structure.

For ferrite-pearlite Fe–V alloy, pearlite phase acts as cathode in the corrosion micro-battery composed of ferrite/pearlite phases, while polygonal ferrite with low electrode potential as anode [21]. As shown in Tables 2 and 3, the smaller area fraction of pearlite phase was, the smaller area ratio of pearlite (cathode) to ferrite (anode) was, and the lower corrosion rate of the tested samples was. The main reason is that reducing pearlite area can prevent cathode process and weaken corrosion driving force [22]. In the lamellar pearlite structure, ferrite lamellae (anode) and cementite
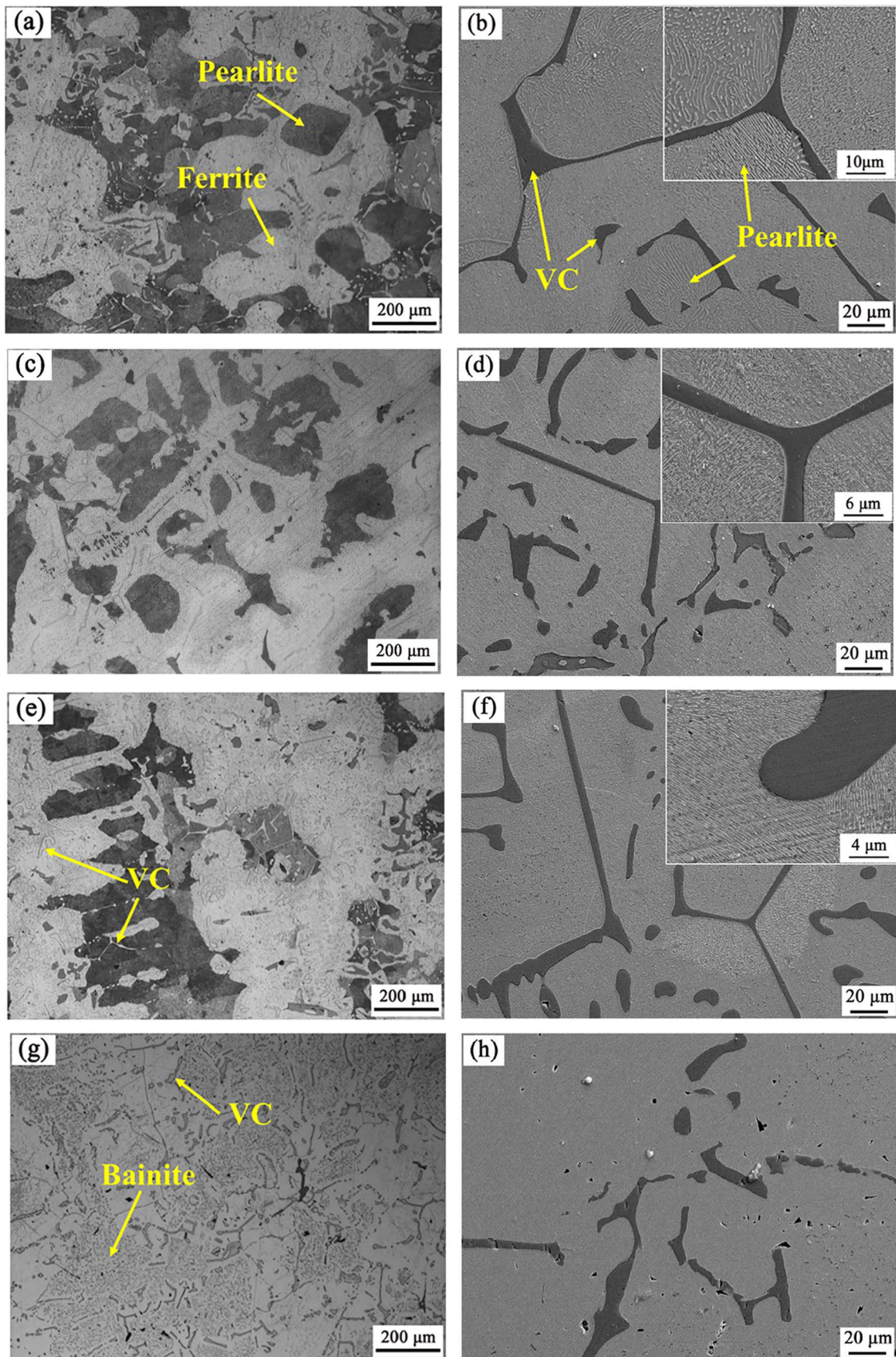
Fig. 1 Optical (left) and field-emission scanning electron (right) micrographs of Fe–V alloy samples: **a**, **b** Sample 1, **c**, **d** Sample 2, **e**, **f** Sample 3, **g**, **h** Sample 4. The insets in **b**, **d**, and **f** show higher magnification images of the pearlite

lamellae (cathode) constituted the corrosion micro-couple [23]. The finer pearlite structure promoted the amalgamation of adjacent micro-galvanic cells and the formation of more uniform corrosion mode, which is beneficial to slowing down the dissolution of ferrite lamellae and reducing the corrosion rate [24]. Analogously, the lowest corrosion rate reported for Sample 4 can also be attributed to the change of microstructure. This is discussed in Sect. 3.4.

3.3 Impedance Analysis

Figure 3a shows the Nyquist plots (imaginary vs. real components of impedances) for the four samples in 3.5% NaCl solution. The plots take the form of an incomplete semicircle arc, which shows that the electrode reaction is controlled by the charge-transfer process (electrochemical reaction step) [20]. In addition, the radius of the capacitive arc reflects the complexity of charge transfer: a larger arc radius of capacitive reactance means a larger electron-exchange impedance value of the tested sample, the greater is its resistance to corrosion reaction, and the better is the corrosion resistance. Figure 3a indicates that the capacitive arc of Sample 4 had the maximum radius.

Bode phase and magnitude plots of the samples are shown in Fig. 3b, c, respectively. The Bode phase diagram shows only one peak for the phase angle in the frequency range of 10^{-1}–10^5 Hz, and the maximum phase angle is about 66° (Sample 4). Combined with the single capacitive arc shown in Fig. 3a, it can be inferred that the samples only contained a time constant during the corrosion process, suggesting that the active behavior occurred on the electrode surface [25]. The occurrence of this dissolution reaction was confirmed by a change in color of the working surface, which turned black in the course of the tests. A broad phase angle observed in Fig. 3b indicated the positive effect of V on corrosion mitigation. The magnitudes of the moduli in the high- and low-frequency regions of the Bode magnitude plots in Fig. 3c provide information concerning the solution resistance (R_s) and charge-transfer resistance (R_c), respectively. Modulus values with little difference in the high-frequency region in Fig. 3c can be interpreted as showing that the resistances of the solution were similar; however, the modulus values in the low-frequency region display evident differences. Generally speaking, a larger modulus in the low-frequency region can be understood as indicating greater resistance to charge transfer and lower corrosion tendency of the sample. The positions of the ordinate in the low-frequency regions in Fig. 3c show that the R_c values gradually increase in the following order: Sample 1, Sample 2, Sample 3, Sample 4. The phase angle and impedance modulus curves of Sample 4 are all above the corresponding curves of the other samples, indicating that Sample 4 exhibited preferable corrosion resistance. The more uniform corrosion mode of bainite

promoted an increase in polarization resistance, leading to a decrease in corrosion sensitivity of the sample.

The electrochemical impedance spectra of the four Fe–V alloy samples were fitted using the *Electrochemical circle fit* module of the Nova 1.10 electrochemical software. A classical ternary equivalent circuit (R_s (Q R_c)) was used to fit and analyze the EIS data. As shown in Fig. 3d, here, R_s refers to solution resistance between the reference and working electrodes, Q represents the electrical double-layer capacitance of the working electrode, and R_c represents the charge-transfer resistance. Owing to the dispersion effect in the frequency–response characteristics of the electrical double-layer capacitor due to roughness or inhomogeneity of the surface of the solid electrode in 3.5% NaCl solution, a constant phase-angle element (CPE) Q was introduced into the equivalent circuit to replace the pure capacitor element C [26]. The impedance (Z_Q) of the CPE is defined by Eq. (4) [27]:

$$Z_Q = j\omega^{-n}/Y_0 \tag{4}$$

in which $j^2 = -1$, ω is angular frequency, Y_0 is CPE contant, and n is the exponent of CPE, where $-1 < n < 1$. The value of n designates the degree of deviation of the dispersion effect and is expressed by the degree of semicircle depression presented in the Nyquist diagram. For $n = 0$ implies an ideal resistor; $n = 0.5$ implies Warburg impedance; $n = 1$ or -1 implies fully capacitive or inductive behavior.

The fitting results of each element in the equivalent circuit are presented in Table 4. The numerical range of the chi-squared error function (χ^2) is 0.036–0.334, which indicates that the experimental results are in good agreement with the adopted equivalent circuit diagram.

R_c can be used to characterize the corrosion rate of the sample. For sample 4 with the largest R_c value, the corrosion dissolution rate is the slowest. This is consistent with the analysis of polarization curves in previous work. The electrolyte prepared during electrochemical measurement had the same composition and a constant temperature, so R_s only fluctuated in a small range. The variations of R_c and R_s reflected in Table 4 are in good agreement with those in the Bode diagrams (Fig. 3b, c). The active surfaces of the samples determine the capacitance of a nonideal electrical double layer. The n values of Samples 1, 2, 3, and 4 were 0.669, 0.672, 0.793, and 0.823, respectively. Sample 1 had the smallest n value, indicating that its surface corroded more severely. An increase in CPE exponent n indicated that the surface activity of the tested specimens gradually decreased, and the degree of surface unevenness caused by corrosion improved. For the ferrite-pearlite Fe–V alloy, ferrite and cementite lamellae in the pearlite constitute a corrosion micro-battery, in which ferrite lamellae are dissolved and cementite lamellae

Table 2 Area fraction and interlamellar spacing of pearlite phase existed in the tested samples

Sample	Fraction of pearlite (%)	Ferrite thickness (nm)	Cementite thickness (nm)	Interlamellar spacing (nm)
1	55.48	521.53 ± 37.41	227.39 ± 61.23	748.92 ± 95.97
2	38.57	220.97 ± 64.72	132.58 ± 29.13	353.55 ± 42.39
3	29.19	132.53 ± 35.84	76.70 ± 28.91	209.23 ± 69.46
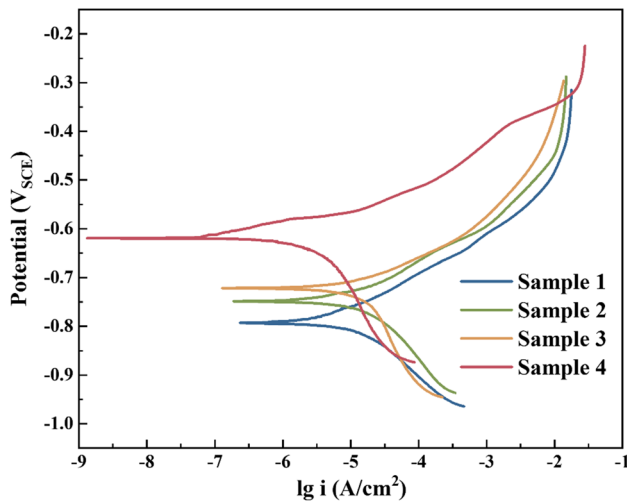
Fig. 2 Polarization diagrams of Fe–V alloy samples in 3.5% NaCl solution

Table 3 Polarization parameters determined from Tafel curves of Fe–V alloy samples in 3.5% NaCl solution

Sample	OCP (V_{SCE})	I_{corr} $(\mu A\ cm^{-2})$	E_{corr} (V_{SCE})	β_a (V/dec)	β_c (V/dec)
1	-0.793	17.572	-0.775	0.074	-0.112
2	-0.748	14.361	-0.736	0.083	-0.154
3	-0.721	12.445	-0.716	0.063	-0.198
4	-0.619	2.104	-0.601	0.051	-0.291

remain. Cementite lamellae accumulated on the surface of the tested samples, which enhanced galvanic corrosion between pearlite and polygonal ferrite. The pearlite was cathodically protected. A decrease in pearlite area means a decrease of cathode area, which corresponds with the metal protection principle of using a large anode and small cathode. This is beneficial in reducing the dissolution loss of anode ferrite, thus improving the unevenness of the surface of the tested samples caused by anode dissolution. Therefore, the value of n showed a gradually increasing trend.

It is widely accepted that alloy elements have significant effect on the corrosion performance. V, Cr and Mn, as carbide-forming elements, have stronger affinity with C than Fe

[28]. Therefore, in the process of pearlite phase transformation, alloying elements aggregated in cementite lamellae by diffusion and combination with C in cementite phases. This resulted in the lower Volta potential of cementite lamellae in finer pearlite and a decrease in the potential difference between cementite and ferrite lamellae [29, 30]. Hence, the finer pearlite structure has better corrosion performance. Accordingly, the corrosion resistance of Sample 1, 2 and 3 improved (Tables 3, 4). Compared with pearlite phase, the lower transformation temperature and the semi-diffusion transformation type of bainite phase promoted the alloying elements uniform distribution in matrix. Due to the homogeneous spatial distribution and good electrochemical stability, Sample 4 with bainite-ferrite structure has the lowest corrosion rate and the best corrosion resistance. Both an increase in the content of V and a decrease in the content of C could bring about the decrease in the number of carbide particles. Therefore, an increase in the concentration of free alloying elements of matrix was beneficial to improving the electrode potential of the matrix [13, 31].

3.4 Corrosion Morphology

The corrosion morphologies of the four specimens after polarization were observed by SEM to further study their specific corrosion behavior. Figure 4 shows FE-SEM micrographs of the samples after electrochemical testing in 3.5% NaCl solution. Their surfaces were covered by corrosion products. The surface corrosion morphology of Sample 1 after polarization (Fig. 4a, b) shows that the matrix structure on the sample surface was completely covered by a thick layer of corrosion products. After polarization, the layer composed of corrosion products on the surface Sample 2 became thinner, as observed in Fig. 4c, d. The corrosion products mainly existed on the pearlite phase and the ferrite phase was only slightly corroded. The layered structure in pearlite promoted galvanic corrosion between ferrite and cementite. Ferritic lamellae dissolved due to their higher corrosion sensitivity; the cementite lamellae, with more noble potential, remained uncorroded on the alloy surface [10, 32]. Partially insoluble cementite lamellae accumulated in pearlite colonies were observed from high-magnification imaging (Fig. 4d) that was not covered by corrosion products. The insert in Fig. 4d shows evidence of cracking on the sample surface. Similar corrosion behavior was observed for
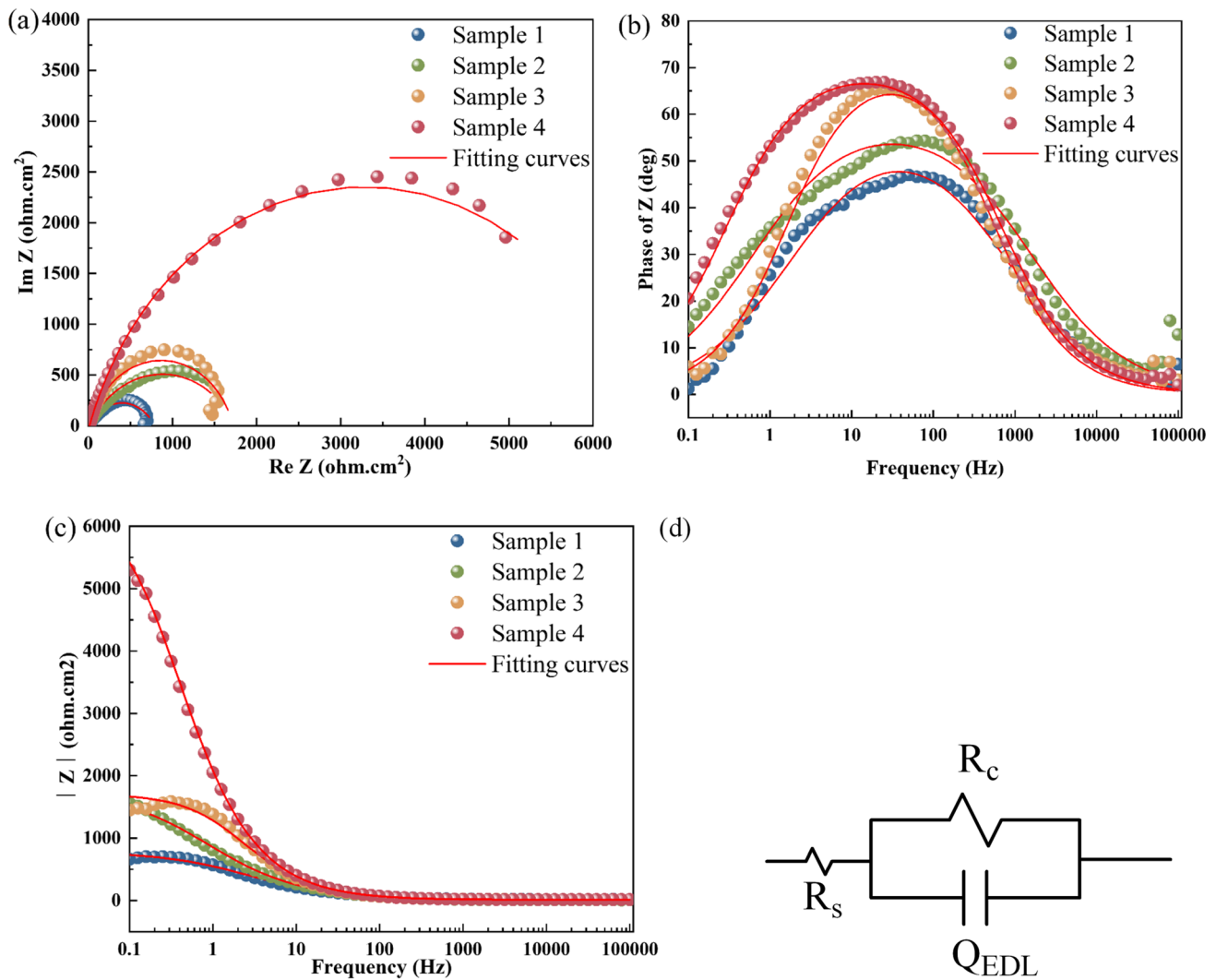
Fig. 3 Electrical impedance spectra for Fe–V alloy samples in 3.5% NaCl solution: **a** Nyquist plots; **b** Bode phase plots; **c** Bode magnitude plots; **d** electrical equivalent circuit

Table 4 Electrical impedance spectra parameters obtained by fitting the equivalent circuit

Sample	R_s, Ω cm^2	CPE, μF cm^2	n	R_c, Ω cm^2	χ^2, Chi squared
1	14.21	115.89	0.66	771.17	0.16507
2	9.01	182.84	0.67	1740.30	0.33431
3	14.40	56.99	0.82	1904.70	0.22845
4	13.50	87.08	0.79	6547.10	0.03657

Sample 3 (Fig. 4e, f), although with a decreasing amount of corrosion products and a more evident lath shape of the cementite. This phenomenon can be reasonably interpreted by the existence of a thinner pearlite structure. On the other hand, a greater amount of corrosion product distributed at the boundary areas of the pearlite colonies in different directions (shown by the arrow in Fig. 4d), which indicates that more corrosion or dissolution occurred at the boundaries between pearlite colonies. As shown in Fig. 4g, h, a slight corrosion attack presented the surface of Sample 4. It is observed that numerous fine cementite particles almost uniformly distributed in the bainite-ferrite matrix (Fig. 1). The fine cementite acted as cathode, while a large area of the bainite-ferrite as anode, which resulted in the slight corrosion of bainite-ferrite (Fig. 4g) [33–35]. The existence of shallow and uniform corrosion pits on the surface of sample (as shown by the arrow in Fig. 4h) indicated that the complete dissolution of bainite-ferrite matrix phases around fine cementite made the central cementite separate from matrix. As shown in Fig. 4i, j, these corrosion products are mainly composed of iron and its oxides by Energy Dispersive Spectrometer.

Fig. 4 Field-emission scanning electron micrographs of Fe–V alloy samples after polarization tests in 3.5% NaCl solution at low (left) and high (right) magnification: **a**, **b** Sample 1, **c**, **d** Sample 2, **e**, **f** Sample 3, **g**, **h** Sample 4; **i**, **j** EDS results of point 1 in **d** and point 2 in **f**
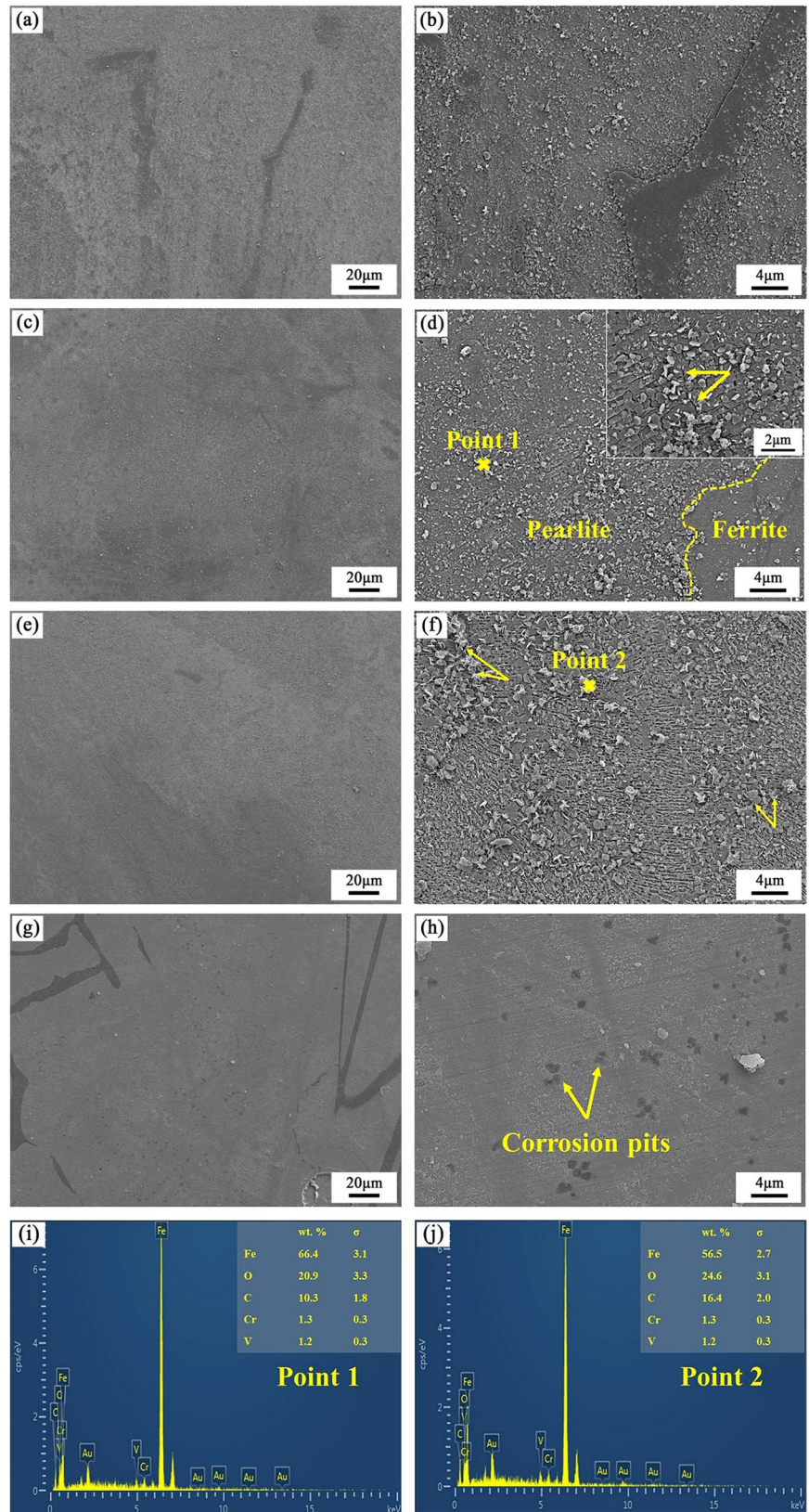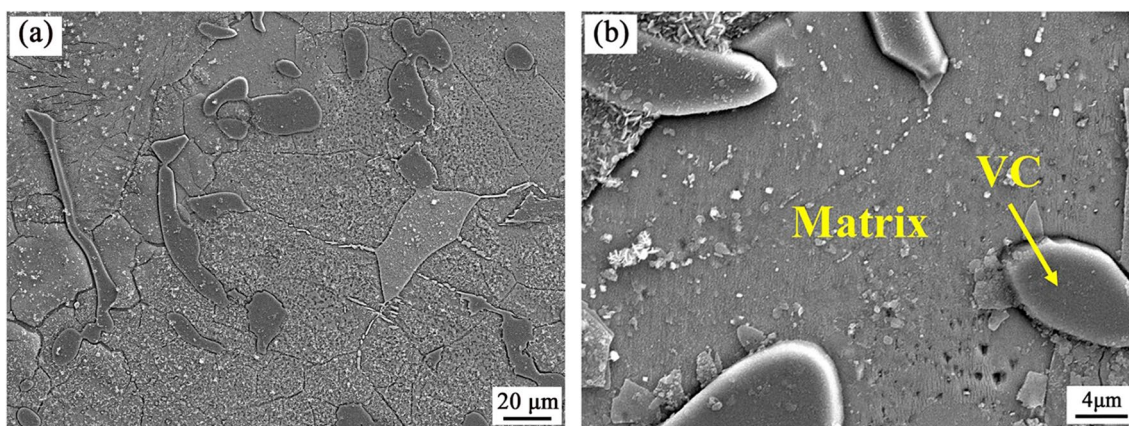
Fig. 5 Scanning electron micrographs of morphological evolution for VC/matrix phase: **a** 500×, **b** 3000×

Figure 5 shows the morphological images of VC/matrix phase after corrosion test. As indicated in Fig. 5a, there were a few corrosion cracks between VC and the matrix. Obviously, the corrosion dissolution existed in the boundary region around VC. However, VC particles remain to be intact. In addition, a distinct morphological height difference between VC and the matrix (Fig. 5b) indicated that the anodic dissolution reaction occurred in the matrix itself. Therefore, the matrix with more negative free corrosion potential acts as anode during the corrosion, while VC as cathode. In brief, the more VC particles are, the stronger the dissolution of the matrix is. This is consistent with results from previous study [36, 37].

4 Conclusions

This study investigated the influence of microstructure on electrochemical properties of Fe–V alloys. The main results are summarized as follows.

(1) Differences in microstructure have a direct bearing on corrosion performance of Fe–V alloys. The results of EIS and potentiodynamic polarization tests suggest that the corrosion resistance of Fe–V alloy in 3.5% NaCl solution increases in the following order: Sample 1, Sample 2, Sample 3, Sample 4. The sample with a bainite phase showed satisfactory corrosion resistance. The I_{corr} of samples with a pearlite phase decreased with a decrease in pearlite content (%). Similarly, thinning of the pearlite interlamellar spacing was beneficial in decreasing the corrosion rate.

(2) Fe–V alloy exhibits active dissolution behavior in 3.5% NaCl neutral solution. The micro-galvanic effect between ferrite and cementite lamellar in the pearlite phase causes the initial corrosion. In addition, more

severe corrosion at the boundaries of pearlite colonies. The bainite phase features uniform corrosion, and the existence of fine cathode cementite promotes shallow corrosion of anode ferrite.

(3) The increase of content of V effectively improves the corrosion resistance of Fe–V alloy. Compared with the matrix, the VC precipitation phase has a more noble corrosion potential so is cathodically protected in the electrochemical corrosion process. Corrosion dissolution between VC and the matrix starts at the junction of VC and the matrix.

Declarations

References

1. C. Garcia-Mateo, L. Morales-Rivas, F.G. Caballero, D. Milbourn, T. Sourmail, Vanadium effect on a medium carbon forging steel. Metals **6**(6), 130 (2016)

2. H. Cao, X.P. Dong, S. Chen, M. Dutka, Y. Pei, Microstructure evolutions of graded high-vanadium tool steel composite coating in-situ fabricated via atmospheric plasma beam alloying. J. Alloy. Compd. **720**, 169–181 (2017)

3. L.A. Smirnov, V.I. Zhuchkov, O.V. Zayakin, LYu. Mikhailova, Complex vanadium-containing ferroalloys. Metallurgist **64**, 1249–1255 (2021)

4. T.N. Baker, Process, microstructure and properties of vanadium microalloyed steels. Mater. Sci. Technol. **25**(9), 1083–1107 (2009)

5. M. Kawalec, E. Fraś, Structure, mechanical properties and wear resistance of high-vanadium cast iron. ISIJ Int. **48**(4), 518–524 (2008)

6. L.J. Xu, S.Z. Wei, J.D. Xing, Q. Wang, Y.Z. Zhang, Microstructure and wear properties of Fe–V–Cr–Mo alloy rolls. Rare Met. Mater. Eng. **36**(A03), 423–426 (2007)

7. M. Kawalec, M. Górny, Influence of carbides morphology on the mechanical properties for Fe–C–V alloys. Int. J. Cast. Metals Res. **29**(1–2), 34–39 (2016)

8. E.S.M. Sherif, H.S. Abdo, N.H. Alharthi, Beneficial effects of vanadium additions on the corrosion of Ti_6Al_xV alloys in chloride solutions. Metals **10**(2), 264 (2020)

9. F. Ozdemir, R.K. Gupta, Influence of vanadium addition on corrosion behavior of high-energy ball milled aluminum alloy 2024. Mater. Corros. **74**(2), 285–292 (2023)

10. T.V. Shibaeva, V.K. Laurinavichyute, G.A. Tsirlina, A.M. Arsenkin, K.V. Grigorovich, The effect of microstructure and non-metallic inclusions on corrosion behavior of low carbon steel in chloride containing solutions. Corros. Sci. **80**, 299–308 (2014)

11. P.J. Wang, L.W. Ma, X.Q. Cheng, X.G. Li, Effect of grain size and crystallographic orientation on the corrosion behaviors of low alloy steel. J. Alloys Compd. **857**, 158258 (2021)

12. S.P. Qu, X.L. Pang, Y.B. Wang, K.W. Gao, Corrosion behavior of each phase in low carbon microalloyed ferrite–bainite dual-phase steel: Experiments and modeling. Corros. Sci. **75**, 67–77 (2013)

13. L.X. Han, C.M. Wang, H.F. Sun, Microstructure and anticorrosion property of high-entropy alloy AlFeNiCrCoTi$_{0.5}$V$_x$. Mater. Trans. **57**(7), 1134–1137 (2016)

14. K.-S. Kim, L.-X. Du, C.-R. Gao, Influence of vanadium content on bainitic transformation of a low-carbon boron steel during continuous cooling. Acta Metall. Sin. (Engl. Lett.) **28**, 692–698 (2015)

15. G. Pant, A.P. Singh, H.K. Sharma, Cooling rate characteristics of vanadium based micro alloyed steel. Mater. Today: Proc. **26**, 1087–1090 (2020)

16. W. Wang, W.B. Wang, Q.R. Sun, Utilization of vanadium slag and iron-rich red mud for the fabrication of Fe–V alloy: mechanism and performance analysis. J. Sustain. Metall. **9**, 341–349 (2023)

17. M. Wang, F.. Zhang, Z. Yang, Effects of alloying elements and cooling rates on the high-strength pearlite steels. Mater. Sci. Technol. **33**(14), 1673–1980 (2017)

18. Y. Li, Z. Yang, The effects of V on phase transformation of high carbon steel during continuous cooling. Acta Metall. Sin. **46**(12), 1501–1510 (2010)

19. S. Liu, F.C. Zhang, Z.N. Yang, M.M. Wang, C.L. Zheng, Effects of Al and Mn on the formation and properties of nanostructured pearlite in high-carbon steels. Mater. Des. **93**, 73–80 (2016)

20. D. Song, J. Hao, F.L. Yang, H.D. Chen, N.N. Liang, Y.Y. Wang, J.C. Zhang, H. Ma, E.E. Klu, B. Gao, Y.X. Qiao, J.P. Sun, J.Y. Jiang, Corrosion behavior and mechanism of Cr–Mo alloyed steel: role of ferrite/bainite duplex microstructure. J. Alloys Compd. **809**, 151787 (2019)

21. A. Rajput, J. Ramkumar, K. Mondal, Cavitation resistance of a Cr-Mn stainless steel, a mild steel, and a high-carbon steel based on rust protectivity and corrosion behavior. J. Mater. Eng. Peform. **31**(1), 439–447 (2022)

22. T. Liu, Y.F. Chen, L.B. Zhu, X.T. Zuo, H.B. Zhang, C. Liu, Effect of alloy adjustment on corrosion resistance of steel rebar. J. Iron Steel Res. **34**(2), 156–161 (2022)

23. C. Liu, X.Q. Cheng, Z.Y. Dai, R.Y. Liu, Z.Y. Li, L.Y. Cui, M.D. Chen, L. Ke, Synergistic effect of Al_2O_3 inclusion and pearlite on the localized corrosion evolution process of carbon steel in marine environment. Materials **11**(11), 2277 (2018)

24. P.K. Katiyar, S. Misra, K. Mondal, Effect of different cooling rates on the corrosion behavior of high-carbon pearlitic steel. J. Mater. Eng. Perform. **27**, 1753–1762 (2018)

25. R. Mech, J. Gasiorek, A. Laszcz, B. Bartosz, Influence of the Nb and V addition on the microstructure and corrosion resistance of the Fe–B–Co–Si alloy. Materials **14**(14), 4045 (2021)

26. D. Sachdeva, R. Balasubramaniam, Corrosion behaviour of Terfenol-D. Corros. Sci. **50**(5), 1340–1352 (2008)

27. B. Panda, R. Balasubramaniam, G. Dwivedi, On the corrosion behavior of novel high carbon rail steels in simulated cyclic wet-dry salt fog conditions. Corros. Sci. **50**(6), 1684–1692 (2008)

28. M. Riebisch, H.G. Sönke, B. Pustal, A.B. Polaczek, Influence of carbide-promoting elements on the pearlite content and the tensile properties of high silicon SSDI Ductile iron. Int. J. Met. **12**, 106–112 (2018)

29. Y. Murase, H. Masuda, H. Katayama, Corrosion resistance of finer/coarser pearlitic structures of carbon steel. J. Electrochem. Soc. **168**(4), 041501 (2021)

30. L.C. Zhou, L.F. Wang, H.Q. Chen, Z.H. Xie, F. Fang, Effects of chromium additions upon microstructure and mechanical properties of cold drawn pearlitic steel wires. J. Mater. Eng. Perform. **27**, 3619–3628 (2018)

31. K. Abd El-Aziz, K. Zohdy, D. Saber, H.E.M. Sallam, Wear and corrosion behavior of high-Cr white cast iron alloys in different corrosive media. J. Bio Tribo Corros. **1**, 25 (2015)

32. Z. Li, W. Xue, Y. Chen, W. Yu, K. Xiao, Microstructure and grain boundary corrosion mechanism of pearlitic material. J. Mater. Eng. Perform. **31**, 483–494 (2022)

33. T. Rojhirunsakool, T. Thublaor, M.H.S. Bidabadi, S. Chandraambhorn, Z.G. Yang, G.H. Gao, Corrosion behavior of multiphase bainitic rail steels. Metals **12**(4), 694 (2022)

34. J. Wei, J.H. Dong, Y.T. Zhou, X.Y. He, C.G. Wang, W. Ke, Influence of the secondary phase on micro galvanic corrosion of low carbon bainitic steel in NaCl solution. Mater. Charact. **139**, 401–410 (2018)

35. Y. Zhang, F. Huang, Q. Hu, Z.X. Peng, J. Liu, Effect of micro-phase electrochemical activity on the initial corrosion dynamics of weathering steel. Mater. Chem. Phys. **241**, 122045 (2020)

36. K. Tokaji, T. Horie, Y. Enomoto, Corrosion fatigue behaviour of high V-Cr–Ni cast irons in 3% NaCl aqueous solution. Int. J. Fatigue **30**(4), 727–733 (2008)

37. N. Çömez, Effect of vanadium on wear and corrosion resistance of Fe–C–Cr hardfacing coatings. J. Mater. Eng. Perform. **32**(4), 1905–1915 (2022)